The rotation rate of cylindrical objects during simple shear

C. Biermeier[a,*], K. Stüwe[a], T.D. Barr[b]

[a]*Department of Geology and Palaeontology, Karl Franzens University, Heinrichstr. 26, 8010 Graz, Austria*
[b]*Department of Earth Sciences, Monash University, Clayton, Vic. 3168, Australia*

Received 16 February 2000; revised 13 September 2000; accepted 13 September 2000

Abstract

The rotational behaviour of circular objects is modelled using a two-dimensional finite element simulation. We present results for linear and non-linear viscous rheologies and explore parameter space for the rheology contrast between object and matrix, η, and for object size relative to the shear zone width, L. For high η, our results confirm analytical descriptions for $L \rightarrow 0$ in that the rotation rate of the object is half of the bulk shear strain rate. However, we show that for $0.1 > L < 0.9$, the rotation rate as a function of L can have a minimum, a maximum, or it can decrease or increase, depending on the stress exponent and η. In fact, for some rheologies, the rotation rate may decrease to <0.3 of the shear strain rate at intermediate $L \approx 0.5$ ($\approx 20\%$ area of porphyroblast in thin section).

These counter intuitive results have important consequences for the interpretation of the rotational behaviour of minerals in deforming rocks. For example, in rocks where garnet constitutes a volumetrically significant proportion of the bulk rock, the effective shear zone boundaries may be given by neighbouring crystals corresponding to intermediate L as described here. Thus, the interpretation of the rotation rate of crystals in such rocks can only be performed if the distance to the effective system boundaries is known. © 2001 Elsevier Science Ltd. All rights reserved.

1. Introduction

The rotational behaviour of rigid objects in a less viscous matrix during deformation has been studied by a number of authors (e.g. Rosenfeld, 1970; Ghosh and Ramberg, 1976; Schoneveld, 1977; Bell and Johnson, 1990; Hayward, 1992; Visser and Mancktelow, 1992; Williams and Jiang, 1999; Ilg and Karlstrom, 2000). This great interest stems from the fact that an understanding of the rotational behaviour may provide handles on two important geological problems: (i) the understanding of the relationship between the rotation and the growth rate of minerals may be a useful tool to estimate the strain rate of rocks that deformed during metamorphism (e.g. Christensen et al., 1994) and (ii) the understanding of the interplay between growth and rotation rate of minerals in a deforming matrix helps to understand non-coaxial fabric development. This is because there is evidence that the disorientation of a homogeneous fabric around rigid objects depends on the size and orientation of these objects (Passchier, 1987). Garnets are the most commonly studied crystals because: (i) their rotational behaviour is relatively simple because of their cubic symmetry

and their strong rheology, (ii) they grow in many common rocks syntectonically during prograde metamorphism at conditions typical of Barrovian metamorphism, and (iii) because garnets appear to preserve inclusion trails very well. Such garnets are well-known as snowball garnets (Fig. 1a) and lend themselves beautifully to the investigation of the rotational behaviour of minerals in natural rocks.

However, there has been some controversy about the interpretation of rotational behaviour of garnets in a deforming matrix as seemingly evident from spiral-shaped inclusion trails. For example, the school of Bell has argued that the foliation in the matrix rotates before being overgrown by the porphyroblast (e.g. Bell et al., 1992a,b; Johnson and Bell, 1996; Hickey and Bell, 1999); while many others have argued that inclusion trails really do record the rotation of porphyroblasts during deformation (e.g. Schoneveld, 1977; Williams and Schoneveld, 1981; Passchier et al., 1992; Mancktelow and Visser, 1993). Bell (1985) suggested that porphyroblasts *do* rotate during simple shear deformation if the shear zone boundaries remain a fixed distance apart, but argued that no spiral inclusion trails form in such environments. He argues that the formation of spiral inclusion trails is limited to environments where shortening across the shear zone boundaries occurs (Bell et al., 1989). Despite this controversy, there have only been few hydrodynamical and numerical studies that have actually

---

* Corresponding author. Tel.: +43-316-380-5682; fax: +43-316-380-9870.

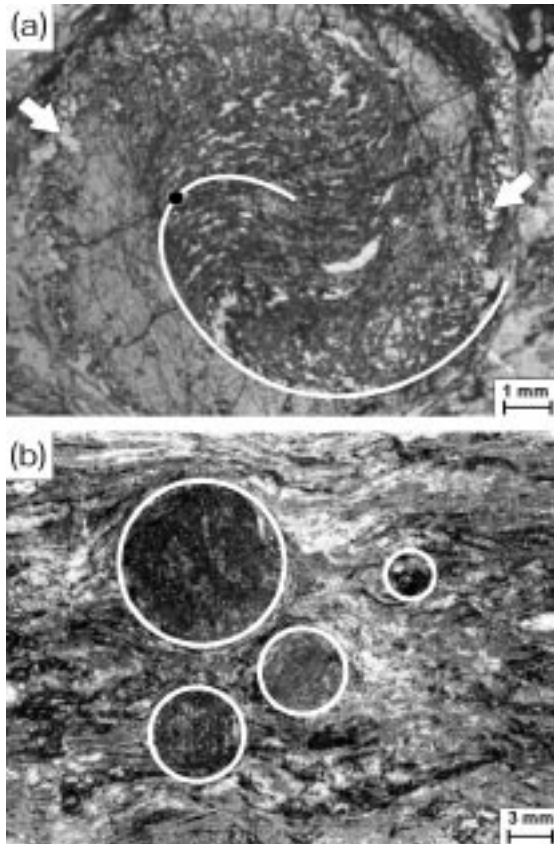*E-mail address:* christian.biermeier@kfunigraz.ac.at (C. Biermeier).

Fig. 1. (a) Natural examples for spiral inclusion trails in a garnet from the Gleinalm complex in the Austroalpine nappe complex, eastern Alps (Austria). According to Schoneveld (1977), such spiral inclusion trails (one being highlighted by the white spiral) are an indicator for syn-deformational crystal growth overgrowing quartz-filled pressure shadows during rotation. The black dot marks the location of maximum curvature of the inclusion trail. White arrows indicate matrix mineral grains penetrating the garnet surface indicating that full coupling between porphyroblast and matrix existed during deformation. (b) Larger view of the garnet-rich mica schist specimen of (a). It may be seen that the distance between crystals is comparable with the crystal diameter. There may be interference between the rotational behaviour of some crystals because neighbouring crystals may act as effective shear zone boundaries hindering or enhancing their rotation rate.

investigated the rotational behaviour of objects as a function of various geologically relevant parameters (Masuda and Ando, 1988; Masuda and Mochizuki, 1989; Bjornerud and Zhang, 1994). In this paper we expand on these studies by investigating the rotational behaviour of circular objects as a function of (i) the size of the object relative to the shear zone boundaries and (ii) a range of finite rheology contrasts between object and matrix.

Our interest in these particular two aspects stems from the following: The *object size* is of relevance because in many garnet-bearing rock types, individual garnet crystals do not lie isolated in an infinite matrix. Garnet porphyroblasts often make up a significant proportion of the rock with the diameter of individual garnet crystals being of the same order as the distance between crystals (Fig. 1b). In such

rocks, the ratio of size to distance between porphyroblasts has been shown to be an important parameter influencing the stress concentration in the matrix (Handy, 1990) and it seems intuitive that the rotation rate of a given garnet crystal will also depend on this interaction. In short, neighbouring crystals may behave as system boundaries enhancing or hindering the rotation rate of a given crystal.

The *rheology contrast* is of relevance because many minerals are not infinitely stronger than their matrix. This is widely known from deforming feldspars, micas and other porphyroblasts (Passchier and Trouw, 1996), but even garnets are thought to behave in a ductile fashion at high grade conditions (Ji and Martignole, 1994, 1996). For example, Kleinschrodt and McGrew (2000) compared the deformation behaviour of garnet, quartz and feldspar and showed that the differences in flow strength are low enough at high grade conditions ($850 \pm 50°C$); so that garnets do deform, depending on the matrix being dominated by feldspar or quartz. However, the observation of ductily deforming garnets has been disputed (den Brok and Kruhl, 1996; Azor et al., 1997). Regardless, as rheological data for garnet are practically unknown, we believe that it is justified to investigate rotational behaviour as a function of finite rheology contrasts (see also Tenczer et al., 2000). In this context we note that many modelling studies have assumed that a rheology contrast of 100 between object and matrix is sufficient to approximate the description of infinitely rigid objects (e.g. Bons et al., 1997) and we will show that this need not be sufficient for some problems.

1.1. Analytical description of rotation—a review

The rotation rate of an infinitely rigid, elliptical object in an infinite matrix of a Newtonian viscous rheology can be described analytically. In two dimensions and during ideal simple shear it is described by:

$$\dot{\omega} = \frac{\dot{\gamma}\left(R^2\cos^2\omega + \sin^2\omega\right)}{R^2 + 1} \tag{1}$$

(Jeffrey, 1922; Ghosh and Ramberg, 1976), where $\dot{\omega}$ is the rate of rotation of the object; $\dot{\gamma}$ is the shear strain rate in the far field given by the time derivative of $\gamma = \tan(\psi)$ where ψ is the angular shear strain (Fig. 2). R is the length ratio of long axis to short axis of the object and ω is the angle of rotation of the object relative to the shear zone boundaries. For circular (or cylindrical) objects, R is equal to 1 and Eq. (1) reduces to the well-known relationship:

$$\dot{\omega} = \frac{\dot{\gamma}}{2} \tag{2}$$

stating that the rotation rate for infinitely rigid objects is half that of the shear strain rate (Rosenfeld, 1970). Eq. (2) can be interpreted in terms of the components of simple shear: in simple shear, half of the angular shear experienced by the pole to the shear zone is a result of rigid rotation and the other half is caused by pure shear at 45° to the shear zone
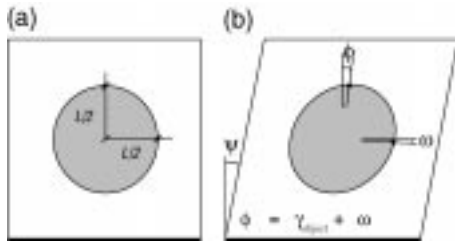
Fig. 2. Illustration of the components of deformation during simple shear of a matrix containing a circular object of finite rheology and diameter L. The shear strain of the matrix γ is related to the angular shear strain ψ by $\gamma = \tan(\psi)$, but is equivalent to ψ at the very small angles used here. The bulk shear strain results in a shear strain of the object γ_{object} and a rotation of the object relative to the matrix ω. Eqs. (2), (3) and (3a) use the time derivatives of the angles shown here. Note that the lines drawn to mark the angles of points on the surface of the object are *not* marker lines, as maker lines become curved during deformation.

boundary (for a good illustration see: fig. 13 in Simpson and De Paor, 1993).

In pure shear, the matrix flow is symmetrical around rigid objects, so that the object does not rotate because of this component of the deformation field (Ghosh and Ramberg, 1976; Simpson and De Paor, 1993). The object rotates only with the rigid body rotational component of the simple shear deformation.

If the cylindrical object has a *finite* rheology contrast to the matrix, then the rotation rate of the object is not a simple function of the far field shear strain rate. Both internal deformation of the object and rigid body rotation relative to the matrix contribute to the displacement of all points of the object. While the object itself deforms to retain an elliptical shape at finite strain (Gay, 1968; Shimamoto, 1975), we consider it impractical to define its overall rotation rate by the rigid body rotational component of object deformation (as suggested for elliptical objects by Ramsey and Huber, 1983, p. 22). This is largely because it would make it difficult to compare the rotation rate of the object relative to that of the matrix. This is particularly because the rigid body rotational component of the matrix deformation is different at all points of the matrix, as our boundary conditions are chosen not to include the far field (see Section 2, Fig. 3). Indeed, because we are investigating boundary effects here, it remains unclear whether the object retains an elliptical shape at finite strain.

For the purpose of this paper we consider an object of finite rheology contrast in a medium subjected to a simple shear strain rate $\dot{\gamma}$. We define the rotation rate of the object $\dot{\omega}$ as the change of angle per unit time of an axis that lies within the eigenvector of the velocity gradient tensor of the far field matrix (the "fabric attractor"—the direction parallel to the shear zone boundary), as this axis does not change orientation because of deformation in the far field. Thus, the rotation rate as defined here is the rotation rate relative to the matrix, but we note that this definition entails a distortional component and a rigid body rotational component. We also define $\dot{\phi}$, which is the rate of change in angle of an axis
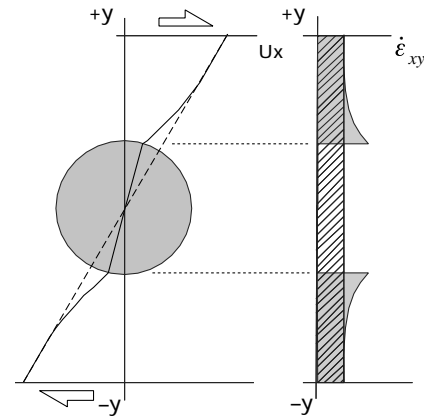

Fig. 3. Schematic illustration showing the velocity field (left) and shear strain rate (right) around a cylindrical inclusion for two end member rheologies. The dashed curves show velocity and shear strain rate if there is no rheology contrast between object and matrix. Then, the velocity gradient across the object is constant and the shear strain rate is also constant. The solid curves show velocity and shear strain rate if the object is rigid (i.e. it is infinitely harder than the matrix). Then, the velocity gradient inside the object will be constant. It is half as large as that of the far field matrix (Eq. (2)). Between the far field matrix and the object contact, there will be a curved section in the velocity gradient. In the problem discussed here, the boundary conditions are imposed in this curved section of the velocity field so that the entire matrix deformation becomes anisotropic.

perpendicular to the shear zone (Fig. 2b). $\dot{\phi}$ incorporates both the angular shear strain rate of the object $\dot{\psi}_{object}$ and the rotation rate of the object relative to the matrix $\dot{\omega}$ and it may be written as:

$$\dot{\phi} = \dot{\psi}_{object} + \dot{\omega}. \tag{3}$$

For small angles, the shear strain rate is virtually equal to the angular shear strain rate $\dot{\psi}_{object} = \dot{\gamma}_{object}$ and Eq. (3) may be written as:

$$\dot{\phi} = \dot{\gamma}_{object} + \dot{\omega}. \tag{3a}$$

If the object is infinitely harder than the matrix, then $\dot{\phi} = \dot{\omega}$ and $\dot{\gamma}_{object} = 0$ and the far field shear strain rate is related to the rotation rate according to Eq. (2). If the object is of the same rheology as the matrix, then $\dot{\omega} = 0$ and $\dot{\gamma}_{object} = \dot{\phi} = \dot{\gamma}$. In the general case discussed here, the rotation rate will be of intermediate values: $0 < \dot{\omega} < \dot{\phi}$ and $0 < \dot{\gamma}_{object} < \dot{\phi}$. It is also true that $\dot{\omega} < \dot{\gamma}/2$ and that $\dot{\gamma}_{object} > \dot{\omega}$ if the object rheology is only slightly higher than the matrix and $\dot{\gamma}_{object} < \dot{\omega}$ if the object is much harder than the matrix.

2. Numerical technique, geometry and boundary conditions

For the purpose of this paper, we assume that rocks behave according to the laws of an incompressible linear or non-linear viscous fluid and we investigate their behaviour in a plane strain environment. The particle velocity and flow paths as well as the distribution of the strain and the
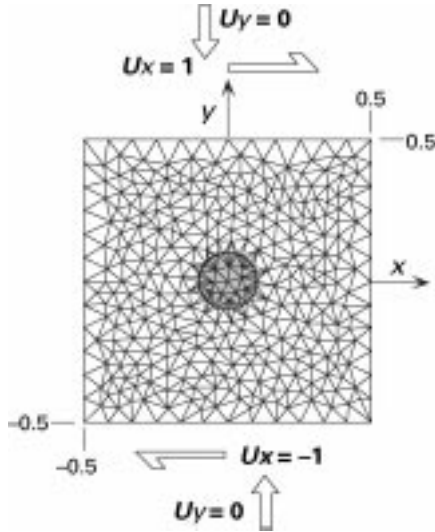
Fig. 4. The finite element grid used in the model calculation labelled with "fixed plate boundary conditions". The shaded region indicates an object of different rheology from the matrix. The shown object size is $L = 0.2$. For smaller inclusions, a mesh with more elements and more nodes along the circumference of the object was used. The rotation rate of the object was calculated from the displacement of the coordinate $x = L/2$ and $y = 0$.

stress field during deformation have been solved using the two dimensional finite element code BASIL (Barr and Houseman, 1996). In summary, this program solves the force balance equations in two dimensions. These may be written as:

$$\frac{\partial}{\partial c_j} \tau_{ij} + \frac{\partial}{\partial c_i} p = 0 \qquad (4)$$

where the i or j subscripts represent the x- and y-directions and c is a general spatial coordinate defined by i or j. τ_{ij} are the ijth components of the deviatoric stress tensor and p is pressure. In order to assign deformation to the stresses obtained from these equations, a constitutive relationship is assumed in which the components of deviatoric stress are related to strain rate by the non-linear relationship:

$$\tau_{ij} = B\dot{E}^{\left(\frac{1}{n}-1\right)} \dot{\epsilon}_{ij}. \qquad (5)$$

In this equation $\dot{\epsilon}_{ij}$ are the components of the strain rate tensor, $\dot{E}$ is the second invariant of the strain rate tensor and the constant B includes all material- and temperature-dependent parts of the rheology (England and McKenzie, 1982). Eq. (5) is a general two-dimensional form of a non-linear relationship between stress and strain rate where n is the stress or power-law exponent defining the non-linearity and the effective viscosity is assumed to be isotropic with respect to the strain rate. The strain rate is defined in terms of the x- and y-direction components of velocity u:

$$\dot{\epsilon}_{ij} = \frac{1}{2}\left[\frac{\partial u_i}{\partial c_j} + \frac{\partial u_j}{\partial c_i}\right]. \qquad (6)$$

Note that $\dot{\epsilon}_{ij}$ in the far field is equivalent in its value to $\dot{\gamma}/2$ when $i \neq j$. For many geological applications, B in Eq. (5) has been shown by deformation experiments to depend inverse-exponentially on temperature (according to the Arrhenius relationship) and can be described with three material constants: an activation energy, a pre-exponential constant and n (e.g. Shelton and Tullis, 1981; Carter and Tsenn, 1986). From Eq. (5) it may be seen that, when $n = 1$, B is the proportionality constant between stress and strain rate and is called viscosity. Eq. (5) then describes a Newtonian fluid behaviour. When $n > 1$, the viscosity depends on strain rate. Then, it is only possible to define an effective viscosity that is given by the ratio of stress and strain rate:

$$\eta_{(eff)} = B\dot{E}^{\left(\frac{1}{n}-1\right)}. \qquad (7)$$

In order to define a viscosity contrast, η, between object and matrix when $n > 1$, we assume that this is given when the stresses are equal and can be described by:

$$\eta = B^n. \qquad (8)$$

More detailed justification of Eq. (8) and its derivation from Eq. (7) is provided by Bons et al. (1997); Tenczer et al. (2000). n is assumed to be same for object and matrix, although we acknowledge that other studies have shown that variation of n between object and matrix can also influence some aspects of the object behaviour (Kenkmann and Dresen, 1998).

2.1. Meshing and initial geometry

The initial geometry of the grid includes a circular region which we call "object" with the diameter L centred in a square box of length 1 (Fig. 4). In the following, the terms "top", "bottom", "left" and "right" will refer to the co-ordinate system as shown in Fig. 4. The object was assigned a rheology contrast η to the matrix according to Eq. (8). This rheology contrast was explored for $\eta = 100$, $\eta = 10$ and $\eta = 2$ both for $n = 1$ and $n = 3$, which was chosen because many rocks appear to behave roughly according to this relationship (Tullis et al., 1991). This geometry was triangulated with a self-triangulation routine using Delauney triangles. Maximum triangle size and minimum mesh angles were prescribed so that numerical resolution was high and stability ensured. The size of the object was varied between $L = 0.1$ and $L = 0.9$, corresponding to an areal proportion of the circular object in the grid between ~0.8% and ~63%. For much smaller and larger objects, the numerical solutions became unstable, but the results are sufficient as the rotation rate for $L \rightarrow 0$ is given by Eq. (2). The rotation rate at $L = 1$ is directly controlled by the boundary conditions and is of no direct interest here. It was explored by Spry (1963). The rotation rate was calculated from the angle change that the coordinate $x = L/2$ and $y = 0$ undergoes per unit time (Figs. 2 and 4). $\dot{\phi}$ was

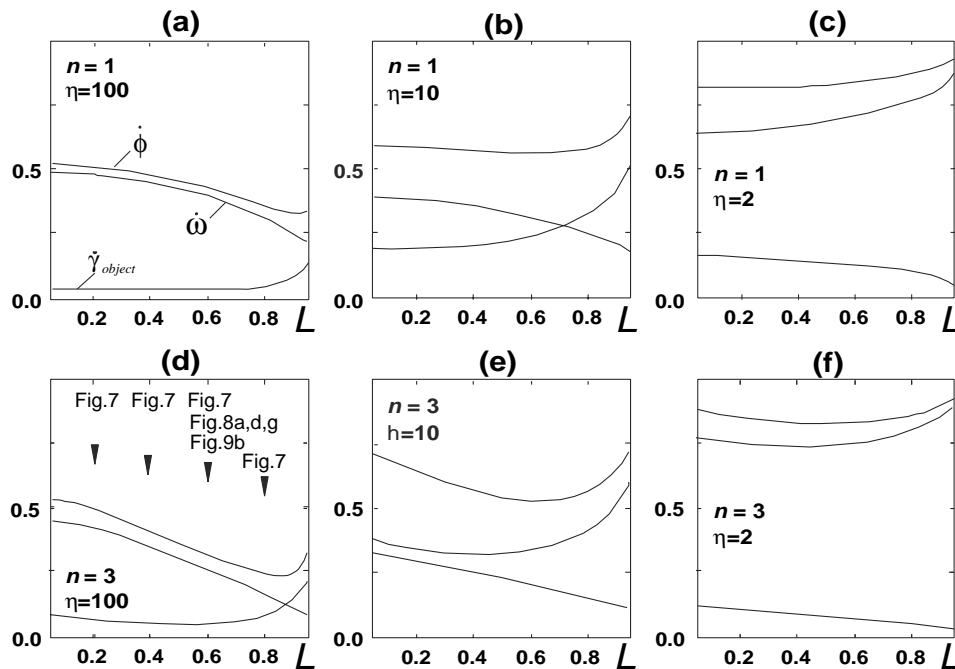## fixed plate boundary conditions

Fig. 5. Results of the model calculations for fixed plate boundary conditions. All diagrams show the rotation rate $\dot{\omega}$, (dotted lines); the shear strain rate of the object $\dot{\gamma}_{\text{object}}$, (dashed lines) and the sum of both $\dot{\phi}$ (continuous lines), normalised to the shear strain rate of the matrix, $\dot{\gamma}$. These parameters are shown as a function of object size L which was sampled at 17 discrete intervals between $0.1 < L > 0.9$. Viscosity contrasts and stress exponents are labelled in each diagram; the three different rates shown are only labelled in (a).

calculated from the velocity of the coordinate $x = 0$ and $y = L/2$ at time $= 0$. From this, the shear strain rate of the object, $\dot{\gamma}_{\text{object}}$, was estimated with Eq. (3a). Progressive rotation rates at finite deformations were not explored.

2.2. Boundary conditions

Numerical simulations were performed for two different sets of boundary conditions approximating simple dextral shear in the far field which describe two different geologically relevant situations. In both sets of boundary conditions, we assumed a horizontal shear velocity at the top and bottom boundaries. The top boundary is moving with velocity $u_x = 1$ towards the right and the bottom boundary is moving with $u_x = -1$ towards the left. For the sides of the grid we assumed "ring" boundary conditions so that the left and right margins of the grid are assumed to join to form a continuum. This assumption simulates an infinite lateral extent of the shear zone with a repeating inclusion geometry. The two sets of boundary conditions differ with respect to the assumptions along the top and bottom boundaries.

In the *first* set of boundary conditions we assumed rigid top and bottom boundaries. As such, these boundary conditions are most comparable with the situation in shear-box experiments, where rigid boundaries on all sides exist, or with natural shear zones that are bound by rigid plates. We

will call these boundary conditions below "fixed plate boundary condition".

With the *second* set of boundary conditions we have simulated shear zones with boundaries that are allowed to bend outwards as a function of the stresses arising in the grid. For this, we defined a constant normal stress at the top and bottom boundaries, rather than zero velocity. We will call these boundary conditions "constant stress boundary condition".

3. Results

Results of the model calculations are shown for the rotation rate of the object, $\dot{\omega}$, its shear strain rate, $\dot{\gamma}_{object}$ and the sum of both as given by $\dot{\phi}$. All three components are shown in Fig. 5 for fixed plate boundary condition and in Fig. 6 for constant stress boundary conditions. Results are normalised to the shear strain rate of the matrix, $\dot{\gamma}$. As we can see by comparing these two figures, there is no simple relationship between the viscosity contrast, stress exponent and the normalised object size. However, the results can be grouped into four qualitatively different results, depending on the trend of $\dot{\omega}$ and $\dot{\gamma}_{object}$ as a function of L. These are:

1. $\dot{\omega}$ and $\dot{\gamma}_{\text{object}}$ are more or less constant and independent of L.
2. $\dot{\omega}$ decreases with increasing L but $\dot{\gamma}_{\text{object}}$ is independent of L.
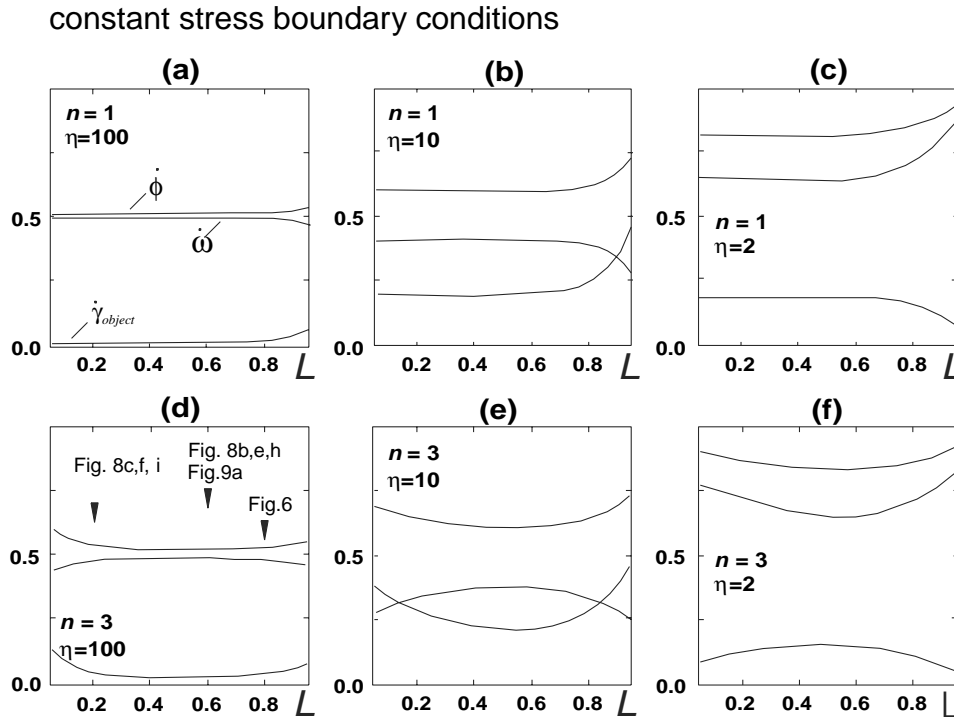
constant stress boundary conditions

Fig. 6. Results of the model calculations for constant stress boundary conditions. All other information for these diagrams are equivalent to that shown in Fig. 5.

3. $\dot{\omega}$ increases and $\dot{\gamma}_{\text{object}}$ decreases with increasing L.
4. $\dot{\omega}$ decreases and $\dot{\gamma}_{\text{object}}$ increases with increasing L.

These four different result groups depend on the stress exponent and viscosity contrast, but relate differently to n and η if the boundary conditions are different. It is therefore necessary to discuss the different result groups individually for the two sets of boundary conditions.

3.1. Fixed plate boundary condition

These results are easiest read by first analysing the case of Newtonian flow (Fig. 5a–c); in particular the case of very hard objects (Fig. 5). There, it can be seen that $\dot{\omega} = 0.5$ for small L, as stated by Eq. (2). Because of the hard rheology of the object, $\dot{\gamma}_{\text{object}}$ is near zero for most L and only trends towards 1 near $L = 1$ where the object is forced to deform by the boundaries. There $\dot{\omega}$ trends to zero. For even harder objects, the bend of the curve for $\dot{\gamma}_{\text{object}}$ becomes even tighter near $L = 1$. However, interestingly, the rotation rate as a function of L decreases long before the shear strain rate begins to increase.

With decreasing viscosity contrast (weaker objects), the rotation rate decreases overall and the shear strain rate of the object increases (Fig. 5b and c). At $\eta = 2$ the rotation rate is around 0.2 for most values of L. At a viscosity contrast of 1 (not illustrated) the rotation rate $\dot{\omega}$ would go to zero and the shear strain rate to one for all L. In contrast to Fig. 5a, where the rotation rate and shear strain rate have different shapes

($\dot{\omega}$ decreases with L while $\dot{\gamma}_{\text{object}}$ stays more or less constant), the shape of the curves becomes more similar at lower η (albeit of opposite sign). Thus, $\dot{\phi}$, being the sum of $\dot{\omega}$ and $\dot{\gamma}_{\text{object}}$, decreases with L at $\eta \gg 10$, but increases with L at $\eta < 10$.

Results for non-linear rheologies (Fig. 5d–f) are only qualitatively similar to the Newtonian behaviour. With respect to their details, they show interesting differences. For example, the rotation rate decreases in a much more linear fashion with increasing L for all viscosity contrasts (Fig. 5d–f). Also, $\dot{\gamma}_{\text{object}}$ is always larger and $\dot{\omega}$ is always smaller than in Newtonian flow. This difference is particularly well-pronounced at intermediate η. An interesting situation is developed for the case of very hard objects at very low L (Fig. 5d). There, the rotation rate is smaller than 0.5 when $n > 1$. The qualitative change of the slope of $\dot{\phi}$ as a function of η is developed for both linear and non-linear rheologies. However, at intermediate η (Fig. 5e at the transition from a negative to a positive slope of this curve), the curve does not become flat as in the linear case, but becomes bowl-shaped and roughly symmetric about $L = 0.6$. The pronounced minimum of $\dot{\phi}$ (and also $\dot{\gamma}_{\text{object}}$) at $L = 0.6$ (Fig. 5e) indicates that the shear zone width has a significant influence on the rotation rate of objects, even when the object is removed from the boundaries by a significant proportion of L.

3.2. Constant stress boundary condition

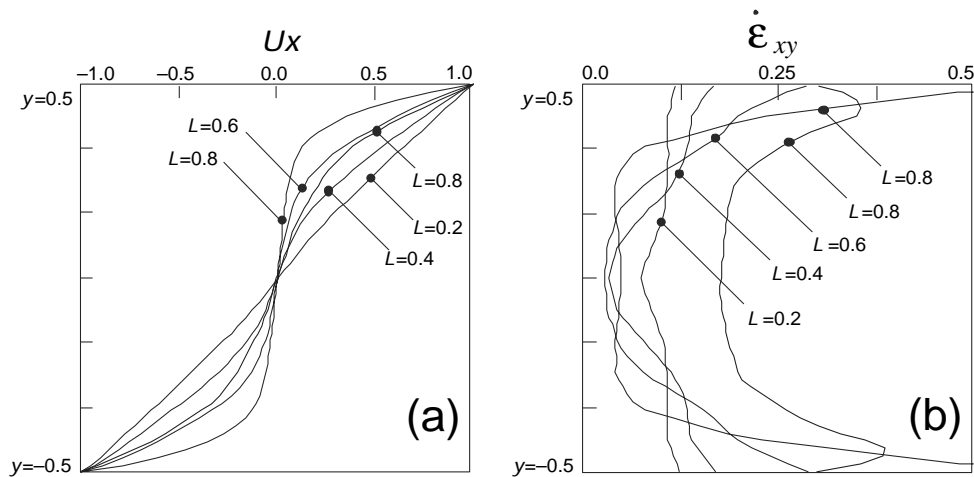In general, the results for constant stress boundary conditions

Fig. 7. (a) *x*-Velocities and (b) shear strain rate (calculated from Eq. (6)) at the margin of the grid (at $x = 0.5$) between $y = 0.5$ and $y = -0.5$. The diagram explains the changes in rotation rate of hard objects ($\eta = 100$) as a function of L as seen in Fig. 5 for the fixed plate boundary conditions (result group 2). Curves are labelled for different values of L. For comparison, one example for $L = 0.8$ is also shown for the constant stress boundary condition (dotted line). Note that for large L the shear strain rate becomes larger on the sides of the object.

(Fig. 6) show that all rate parameters are not such a strong function of L as is the case of the fixed plate boundary conditions (Fig. 5). This is because the material is not forced to flow around the object in a restricted shear zone of constant width, but the boundaries may adjust and bend outwards to maintain constant normal stress along them. Thus, the shear and normal components of stress and strain in the *y*-direction are larger under constant stress boundary conditions than under fixed plate conditions. This leads under linear viscous flow to constant values of $\dot{\gamma}_{object}$, $\dot{\phi}$ and $\dot{\omega}$ over a large range of L. For example, in contrast to Fig. 5a, Fig. 6a shows that $\dot{\omega}$ is near 0.5 for practically all L and the shear strain rate $\dot{\gamma}_{object}$ is negligible. Clearly, as for all figures, $\dot{\omega}$ goes to zero and $\dot{\gamma}_{object}$ to one at $L = 1$ but the change of both values occurs much closer to $L = 1$ than in Fig. 5a.

At lower viscosity contrasts (Fig. 6b and c), the rotation rate decreases and the shear strain rate increases, but both parameters remain constant for a larger range of L than for the corresponding parameter range on Fig. 5a–c. Because of this, $\dot{\phi}$ does not change qualitatively as on Fig. 5a–c, but only increases in slope with decreasing η.

For $n = 3$ (Fig. 6d–f), $\dot{\omega}$ shows a maximum and $\dot{\gamma}_{object}$ a minimum at intermediate L for all η. This is completely different from all other results presented here, where the highest rotation rate has been always been given by the lowest object sizes! Here, the highest rotation rate is given at about $L = 0.5$. At higher η, the maximum of $\dot{\omega}$ shifts to lower L. For smaller *and* for larger objects, $\dot{\gamma}_{object}$ increases and $\dot{\omega}$ decreases. The rotation rate at low L departs significantly from the case of the fixed plate boundary condition shown in Fig. 5 and also from its value for Newtonian flow as given by Eq. (2). For example, for very hard objects, the rotation rate at small L is only about 0.4 (Fig. 6d).

3.3. Interpretation of results

The curves for $\dot{\omega}$, $\dot{\gamma}_{object}$ and $\dot{\phi}$ shown in Figs. 5 and 6 illustrate a number of counter-intuitive features that need to be explained. In particular these are: (i) why does the rotation rate and $\dot{\phi}$ decrease with increasing L while $\dot{\gamma}_{object}$ remains constant for hard objects and fixed plate boundary conditions at all n (result group 2; Fig. 5a,d)? (ii) why does $\dot{\omega}$ increase with increasing L (up to about $L < 0.5$) for constant stress boundary conditions and non-linear viscosities (result group 3; Fig. 6d–f)? (iii) why, at very high viscosity contrasts, is $\dot{\omega}$ smaller than 0.5 for $L \rightarrow 0$ in non-linear rheologies, regardless of the boundary conditions? The other result groups (group 4; Fig. 5b,c,e,f and group 1; Fig. 6a–c) are straightforward to interpret: the decrease of $\dot{\omega}$ with increasing L at decreasing viscosity contrasts and is a mere function of the increasing dominance of deformation of larger objects when they are soft. These results are intuitively explained and will not be discussed further here.

Question (i) is relatively easy to explain. For small inclusions (Fig. 5a), there is a mostly linear velocity gradient between the top and the bottom boundary. For larger L, the velocity gradient becomes smaller on the sides of the inclusion and becomes larger in the narrow seams between the object and the boundaries (Fig. 7). Effectively, the object starts acting like a rigid band in the middle of the grid, while the areas near the top and bottom boundaries partition the strain. Small shear zones start forming around the object. This is illustrated in Fig. 7a where it can be seen that the *x*-velocity (u_x) decreases towards the centre of the grid more rapidly for large objects, than for small objects. Fig. 7b illustrates this by plotting the shear strain rate, which is largely the *x*-velocity gradient in the *y*-direction, as it may be interpreted from Fig. 7a. Small differences between Fig. 7b and the slope of the curves in Fig. 7a arise from the
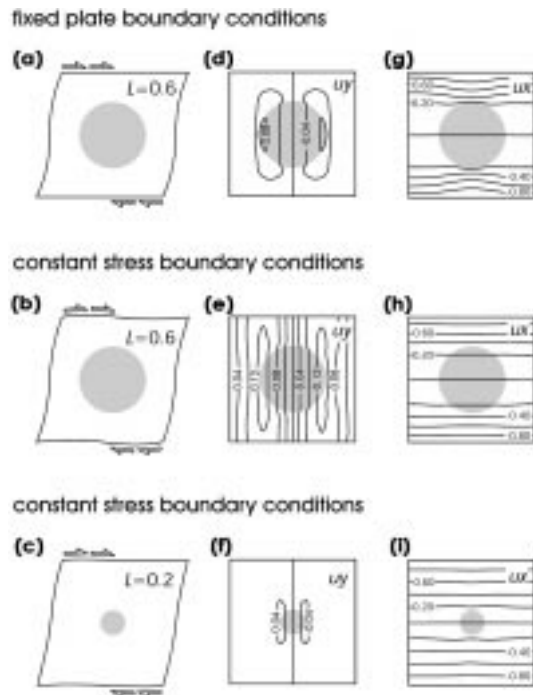
fixed plate boundary conditions

(a) ... L=0.6 (d) ... uy (g) ... u,x

constant stress boundary conditions

(b) ... L=0.6 (e) ... uy (h) ... u,x

constant stress boundary conditions

(c) ... L=0.2 (f) ... uy (i) ... u,x

Fig. 8. Schematic sketches as well as *x*-velocities and *y*-velocities for some examples of fixed plate and constant stress boundary conditions from Figs. 5d and 6d. The diagram helps to explain the increase in rotation rate with increasing *L* (result group 3). See text for details.

velocity gradient contribution in the *x*-direction to the shear strain rate, according to the definition of shear strain rate in Eq. (6).

This explanation holds for linear and non-linear viscous rheologies (compare Fig. 5a with d) and the effect becomes less significant for lower viscosity contrasts (compare Fig. 5a with b and c). When the boundary conditions are changed to constant stress conditions, the key feature of result group 2 vanishes as the velocity above and below the object is allowed to partition significantly into an *x*- and a *y*-component (dotted lines in Fig. 7). Thus, the velocity gradient remains much more constant across *y* and the rotation rate is much less dependent on *L*. For any given *L*, $\dot{\omega}$ is therefore larger for constant stress boundary conditions than for fixed plate conditions.

Question (ii) is not so easily explained. The maximum of $\dot{\omega}$ at intermediate *L* (Fig. 6d) is the consequence of the interplay of two different processes. Both processes are related to an increasing effect of the boundary conditions on the rotation rate of the object and occurs in all diagrams of Fig. 6, but it is more pronounced for non-linear rheologies (bottom row in Fig. 6). The *in*crease of $\dot{\omega}$ up to about *L* = 0.5 is caused by an increasing *y*-component of the velocity field imposed by the boundaries. The *de*crease of $\dot{\omega}$ at *L* > 0.5 is caused by the same effect that explains result group 2 (question (i), last paragraph, Fig. 7); that is: the partitioning of the strain into small shear zones on the sides of the object. The fact that the boundary conditions

impose an additional *y*-velocity causing higher rotation rates with higher *L* is illustrated by comparing Fig. 8a–c. Fig. 8b shows that — because the boundaries are allowed to bend outwards — the imposed boundary–parallel velocity has both an *x*- and a *y*-component. The *y*-component of this velocity is clearly larger when the inclusion is large, rather than when it is small, because the boundaries need to bend further out to maintain constant stress (compare Fig. 8b and c; the outwards bending is larger in Fig. 8b). This is quantified in Fig. 8e and f and is the cause for higher rotation rates at higher *L*. The difference in rotation rate between *fixed plate* and *constant stress* boundary conditions at any given *L* is caused by the same effect (compare Fig. 8d and e or Fig. 5d and Fig. 6d). In Fig. 8d the *y*-component of the velocity field along the circumference of the object is much smaller than in Fig. 8e because in the former the top and bottom of the shear zone are fixed in *y*. Thus, for both cases, the decrease of $\dot{\omega}$ is caused by a decrease of imposition of a *y*-component of velocity: in the case of Fig. 8f (in comparison with Fig. 8e) this is because the object is further away from the boundary, and in the case of Fig. 8d (in comparison with Fig. 8e) it is because the boundary condition is changed. For *L* > 0.5, the rotation rate decreases because the effect of strain partitioning wins over the effect discussed above. This becomes clear from Fig. 8g–i, where the same effect discussed in Fig. 7 may be seen in terms of contoured *x*-velocities.

The answer to question (iii), the cause for rotation rates $\dot{\omega} < 0.5$ for *L* → 0 (see Figs. 5d–f and 6d–f), lies in the non-linearity of the rheological behaviour, because it does not occur at *n* = 1. However, Masuda and Mizuno (1996) concluded that the rotation rates of infinitely rigid objects at *L* = 0 is $\dot{\omega} = 0.5$ for *n* = 1–5. Thus, we suggest that our result lies in the fact that a rheology contrast of $\eta = 100$ is insufficient to approximate the behaviour of rigid objects. This is confirmed by the fact that $\dot{\gamma}_{object}$ has appreciable values at *L* → 0. In fact, it may be seen that $\dot{\gamma}_{object}$ decreases with increasing *L*. This decrease is probably a function of the effect that the boundary conditions influence the rotation rate the most at intermediate *L*. While we suspend our full interpretation of this question, we emphasise the importance of this result: In non-linear viscous materials the rotation rate of objects may be lower than half of the shear strain rate, even if they are of the order of 100 times stronger than the matrix.

4. Discussion

The model calculations presented and interpreted above have some important implications for the interpretation of rotation rates of porphyroblasts in rocks. However, they have been performed making a number of simplifying assumptions. It is therefore necessary to discuss these limitations before going onto some geological interpretations.

4.1. Limitations of geological application

Cylindrical geometry: the results presented here were performed in two dimensions and can therefore only be applied directly to cylindrical objects, for example needle-shaped mineral grains. However, in geological studies, garnets (with an approximately spherical shape) are best for inferring rotation rates for reasons outlined in the introduction of this paper. While we are confident that all effects hindering or enhancing the rotation rates as discussed in the last section are also relevant to spherical objects, the L of the two-dimensional objects discussed above cannot be translated directly into the diameter of a spherical grain as measured in thin section. Rather, L must correspond to some average diameter measured perpendicular to the rotation axis and averaged over the length of the rotation axis. In a sphere, this is given by $L \approx D\pi/4$, where D is the diameter of the sphere. Thus, we suggest that the rotation rate of spherical objects may be approximated by our calculations using an $L \approx 0.78D$. For the relationship between sphere diameter and apparent diameter in thin section we refer to the method of Ehlers et al. (1994).

Finite deformation: the results presented above are valid only for an incremental time step at the onset of deformation. Clearly, the rotation rates will change dramatically as soon as the object becomes non-circular (see Ghosh and Ramberg, 1976; Passchier, 1987; Simpson and De Paor, 1993). Thus, our results may be valid for finite deformation only for hard objects (like those approximated in Figs 5a,d and 6a,d). Therefore, our geological discussion below will focus only on rotation rate changes as a function of L for objects with very high rheology contrasts to the matrix.

Object–matrix coupling: in our calculations, we have assumed a continuum between object and matrix so that there is 100% coupling between inclusion and matrix. We note that Kenkmann and Dresen (1998) showed that the reduction of coupling has a great influence on the differential stress distribution and therefore also probably on the rotation rate. While we acknowledge that decoupling between porphyroblasts and matrix has been observed in rocks (Odonne, 1994), we note that in many garnet crystals containing spiral inclusion trails, matrix crystals penetrate the surface of the rotating crystal (white arrows in Fig. 1a) so that full coupling is ensured.

Deformation mechanism: our results were obtained for an incompressible viscous material and no consideration was given to elastic deformation or other grain-scale deformation processes. As we know from deformation maps for different minerals there are a lot of grain and phase boundary processes influencing the occurring strain rate and stress values, for example strain hardening, metamorphism of the matrix and many others. While it goes far beyond the scope of this paper to explore the influence of such mechanisms, we note that our results may only be used for a meaningful interpretation if the assumption of a viscous material is approximated.

4.2. Geological relevance

Despite the limitations discussed in the last section, we believe that our results have some relevance to the interpretation of rotation rates of porphyroblasts in rocks. In particular, we will focus below on the fact that the rotation rate of circular porphyroblasts in a viscous matrix need not stay constant but may change as a function of L. This very general result has been true for *all* rheology contrasts, *all* power law exponents and is independent of the boundary conditions explored here (*all* curves on Figs. 5 and 6 change as a function of L). Thus, while refraining from a quantitative interpretation of Figs. 5 and 6 in real rocks, we will use this general result to present some warnings about the interpretation of rotating porphyroblasts.

Shear zones in rocks are rarely of the width of individual crystals contained in them. However, in coarse-grained garnet–mica schists (in which the distance between individual crystals is comparable with the crystal size (e.g. Fig. 1b)), neighbouring garnet crystals may act as "effective shear zone boundaries" to a particular garnet of which the rotational behaviour may be under consideration. 20% of garnet porphyroblast per area of thin section is common to many coarse-grained pelitic rocks so that the effect of neighbouring crystals cannot be excluded (in our grid with the side length 1, the areal proportion of object per area is given by $(L/2)^2\pi$ so that L between zero and 1 corresponds to an areal proportion of garnet in a thin section between 0 and 78%). As a consequence, the rotational behaviour of individual crystals may vary dramatically, depending on, for example, grain size or relative growth rates. As crystals in many coarse-grained garnet mica schists grow during a continuous *PT*-deformation evolution of the rock, L may change during the evolution of the *PT* path. Thus, the rotation rate may also change over time, even if the overall deformation regime remains constant. As a result, inclusion trails in porphyroblasts of different size, or in porphyroblasts that nucleated at different time steps of the same *PT* evolution may contain very differently-shaped inclusion trails. In fact, in rocks where some garnet crystals ultimately touch, it is conceivable that the entire evolution of rotation rate from $L = 0$ to $L = 1$ is seen by some crystals.

As an example, reconsider the marked inclusion trail in Fig. 1a. This trail has its maximum curvature at the location marked by the black dot. Assuming a constant radial growth rate (note that this assumption implies a *decreasing* volumetric growth rate) this might be interpreted as a maximum in the rotation rate and ultimately as a maximum in the shear strain rate of the rock. Our calculations show that this maximum in rotation rate may merely reflect a growth path from $L \approx 0.1$ towards $L \approx 0.8$ on Fig. 6d or e. Clearly, such interpretations may only be made if the radial growth rate as a function of time is understood. This involves a careful petrological investigation.

L may not only increase during crystal growth in a constant width shear zone (discussed in the last paragraph),
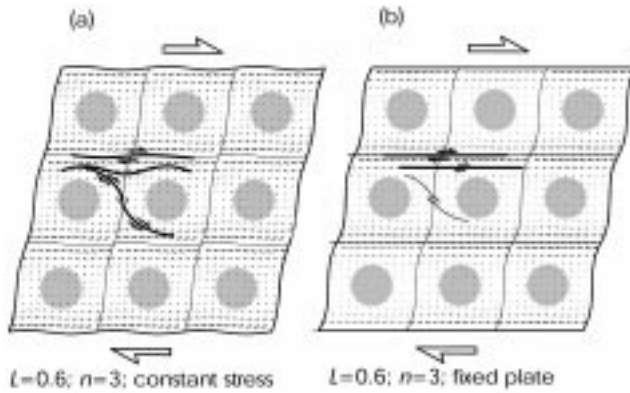
Fig. 9. Illustration of differences of the velocity field around objects ($\eta = 100$) as a function of different boundary conditions. The small arrows are vectors showing direction and magnitude of the velocities relative to the centre of each porphyroblast. In order to simulate the feel of a "real" thin section, a total of nine identical model calculations were pasted together. This is allowed because of symmetry reasons. Note however that this figure should not be misinterpreted by inferring velocity gradients across the continuous lines which separate individual (identical) model runs. Some obvious differences between the developing fabrics are discussed in the text. The strain partitioning discussed in Fig. 7 can be seen clearly on Fig. 9b.

but L may also increase if the crystal size stays constant and the shear zone narrows in width. This may be given in a general shear environments, for example during folding where limb attenuation and hinge thickening may cause an additional effect influencing the rotation rate of crystals, in addition to the changes of shear strain rate in different geometric positions around a fold (Visser and Mancktelow, 1992). In this sense, the pure shear component of general shear may have an indirect influence on the rotation rate by changing the effective shear zone width. Interestingly, this interpretation is in support of Bell et al. (1989), in that the rotation rate of garnet crystals may be slowed in general shear environments where the convergence of the shear zone boundaries causes an increase of L from near zero to intermediate values.

When comparing Figs. 5 and 6 we have shown that the boundary conditions have an important influence on the rotation rate. Thus, when attempting to determine rotation rates from natural examples, it is crucial to understand the relevant boundary conditions. How the difference between the two sets of boundary conditions investigated here may be recognised in the fabric of rocks is illustrated in Fig. 9. There, the velocity field in and around objects with a rheology contrast to the matrix of $\eta = 100$ is plotted using an intermediate $L = 0.6$ where the difference between the two boundary conditions is large (compare Fig. 5d and Fig. 6d) and the rotation rate for the constant stress boundary condition is near its maximum (Fig. 6d). As the shear strain rate will be the principle cause for fabric development (i.e. velocity gradients in the x- and y-directions; see Eq. (6)), this velocity field may be used to infer the fabric that may be seen in a rock (see also Fig. 7) (for other causes

of fabric development see Lister and Williams, 1983). Note that Fig. 9 should not be misinterpreted as the velocity field is drawn *relative to the centre* of each of nine porphyroblasts in this figure (separated by continuous lines). Thus, reversals in the velocity field across these lines are only apparent. Nevertheless, it may be seen that the principle fabric development will be parallel to the x-coordinate as there is practically no gradient in the length of the velocity vectors in the x–direction.

Fig. 9 shows that we can decide from the shape of the foliation around porphyroblasts which boundary conditions are relevant. When *constant stress* boundary conditions prevail, an anastomosing fabric will be developed around porphyroblasts. *No straight* fabric elements will be developed (Fig. 9a). When fixed plate boundary conditions prevail, the strain and fabric development will be partitioned largely into *straight* "sub-shear zones" between porphyroblasts and there will be very little strain (and shear strain rate) behind and in front of the porphyroblasts (Fig. 9b). Effectively, a "layered" system should be observed where the porphyroblasts hinder the fabric development sufficiently so that the strain is accommodated in shear zones between them. In general, the rotation rate of crystals in the example of Fig. 9a will be larger than in that of Fig. 9b.

5. Conclusion

In conclusion, our study has shown that the rotation rate of cylindrical objects in a simple shear environment varies as a function of the object size relative to the shear zone boundaries, which we call L. The rotation rate as a function of L may increase, decrease, it may have a maximum or it may have a minimum. In more detail we have shown that:

1. For linear viscous materials and very high rheology contrasts, our results confirm analytical results for rotation rate for $L \rightarrow 0$ and for $L = 1$. For $L \rightarrow 0$ the rotation rate is $\dot{\omega} = 0.5$ (Ghosh and Ramberg, 1976; Simpson and De Paor, 1993) and for $L = 1$ the rotation rate goes towards zero (Spry, 1963). There, all the shear imposed by the boundaries is taken up in deformation of the object.
2. $\dot{\omega}$ becomes significantly smaller than 0.5 at $L > 0.3$, even for objects of high rheology contrast to the matrix. This is because the strain gets partitioned in the regions near the shear zone boundaries and the region around the object behaves like a rigid band in the middle of the grid. This feature also occurs in non-linear viscous materials.
3. When the shear zone boundaries are maintained at constant stress, the partitioning of the strain into the regions near the boundaries competes with an increasing component of the velocity field in direction normal to the shear zone boundaries. This competition results in a maximum of the rotation rate at intermediate object

sizes. This effect is particularly pronounced in non-linear viscous materials.

4. In non-linear viscous materials, the rotation rate may become $\dot{\omega} < 0.5$ for $L \rightarrow 0$ for all rheology contrasts $\eta < 100$. We suggest that this indicates that $\eta = 100$ is not sufficient to describe the behaviour of rigid objects.

5. There is a general trend that, with decreasing viscosity contrast, the shear strain rate of an object increases and the rotation rate decreases. However, the decrease in rotation rate is not related *directly* to the decrease in the viscosity contrast. For example, objects of $\eta = 2$ still have an appreciable rate of rotation. Correspondingly, even at a viscosity contrast of $\eta = 100$, objects still have a significant shear strain rate for some rheologies and boundary conditions. This is also the cause of conclusion 2.

6. Quantitative application of our results to real rocks is difficult. However, the results show that there should be care taken in making generalised interpretations about the magnitude of rotation rates of porphyroblasts, if the distance to the effective shear zone boundaries is not understood. For example, in metamorphic rocks where garnet growth occurs during deformation, the effective object size may change, so that that the entire spectrum of rotation rates that occur between $L = 0$ and $L = 1$ may be found in a single thin section or even in a single crystal.

Acknowledgements

References

Azor, A., Simancas, J.F., Exposito, I., Lodeiro, F.G., Poyatos, D.J.M., 1997. Deformation of garnets in a low-grade shear zone. Journal of Structural Geology 19, 1137–1148.

Barr, T.D., Houseman, G.A., 1996. Deformation fields around a fault embedded in a non linear ductile medium. Geophysical Journal International 125, 473–490.

Bell, T.H., 1985. Deformation partitioning and porphyroblast rotation in metamorphic rocks: radical reinterpretation. Journal of Metamorphic Geology 3, 109–118.

Bell, T.H., Johnson, S.E., 1990. Rotation of relatively large rigid objects during ductile deformation: well established fact or intuitive prejudice?. Australian Journal of Earth Sciences 37, 441–446.

Bell, T.H., Duncan, A.C., Simmons, J.V., 1989. Deformation partitioning, shear zone development and the role of undeformable objects. Tectonophysics 158, 163–171.

Bell, T.H., Forde, A., Hayward, N., 1992a. Do smoothly curved, spiral-shaped inclusion trails signify porphyroblast rotation? Geology 20, 59–62.

Bell, T.H., Johnson, S.E., Davis, B., Forde, A., Hayward, N., Wilkins, C., 1992b. Porphyroblast inclusion-trail orientation data: eppure non son girate!. Journal of Metamorphic Geology 10, 295–307.

Bjornerud, M., Zhang, H., 1994. Rotation of porphyroblasts in non-coaxial deformation: insights from computer simulations. Journal of Metamorphic Geology 12, 135–139.

Bons, P.D., Barr, P.D., ten Brink, C.E., 1997. The development of δ-clasts in non-linear viscous materials: a numerical approach. Tectonophysics 270, 29–41.

den Brok, B., Kruhl, J.H., 1996. Ductility of garnet as an indicator of extremely high temperature deformation: discussion. Journal of Structural Geology 18, 1369–1373.

Carter, N.L., Tsenn, M.C., 1986. Flow properties of continental lithosphere. Tectonophysics 136, 27–63.

Christensen, J.N., Selverstone, J., Rosenfeld, J.L., DePaolo, D.J., 1994. Correlation by Rb–Sr geochronology of garnet growth histories from different structural levels within the Tauern Window, Eastern Alps. Contribution to Mineralogy and Petrology 118, 1–12.

Ehlers, K., Powell, R., Stüwe, K., 1994. Cooling histories from garnet—biotite equilibrium. American Mineralogist 79, 737–744.

England, P.C., McKenzie, D., 1982. A thin viscous sheet model for continental deformation. Geophysical Journal of the Royal Astronomical Society 70, 295–321.

Gay, N.C., 1968. Pure shear and simple shear deformation of inhomogenous viscous fluids. I. Theory. Tectonophysics 5, 211–234.

Ghosh, S.K., Ramberg, H., 1976. Reorientation of inclusions by combination of pure shear and simple shear. Tectonophysics 34, 1–70.

Handy, M.R., 1990. The solid-state flow of polymineralic rocks. Journal of Geophysical Research 95, 8647–8661.

Hayward, N., 1992. Microstructural analysis of the classical spiral garnet porphyroblasts of south-east Vermont; evidence for non-rotation. Journal of Metamorphic Geology 10, 567–587.

Hickey, K.A., Bell, T.H., 1999. Behaviour of rigid objects during deformation and metamorphism: a test using schists from the Bolton syncline, Conneticut, USA. Journal of Metamorphic Geology 17, 211–228.

Ilg, B.R., Karlstrom, K.E., 2000. Porphyroblast inclusion trail geometries in the Grand Canyon: evidence for non-rotation and rotation?. Journal of Structural Geology 22, 231–243.

Jeffrey, G.B., 1922. The motion of ellipsoidal particles immersed in a viscous fluid. Proceedings of the Royal Society of London, Series A 102, 161–179.

Ji, S., Martignole, J., 1994. Ductility of garnet as an indicator of extremely high temperature deformation. Journal of Structural Geology 16, 985–996.

Ji, S., Martignole, J., 1996. Ductility of garnet as an indicator of extremely high temperature deformation: reply. Journal of Structural Geology 18, 1375–1379.

Johnson, S.E., Bell, T.H., 1996. How useful are 'millipede' and other similar porphyroblast microstructures for determining synmetamorphic deformation histories? Journal of Metamorphic Geology 14, 15–28.

Kenkmann, T., Dresen, G., 1998. Stress gradients around porphyroclasts: paleopiezometric estimates and numerical modelling. Journal of Structural Geology 20, 163–173.

Kleinschrodt, R., McGrew, A., 2000. Garnet plasticity in the lower continental crust: implications for deformation mechanisms based on microstructures and SEM-electron channelling pattern analysis. Journal of Structural Geology 22, 795–809.

Lister, G.S., Williams, P.F., 1983. The partitioning of deformation in flowing rock masses. Tectonophysics 92, 1–33.

Mancktelow, N.S., Visser, P., 1993. The rotation of garnet porphyroblasts around a single fold, Lukmanier Pass, Central Alps: reply. Journal of Structural Geology 15, 1369–1372.

Masuda, T., Ando, S., 1988. Viscous flow around rigid spherical body: a hydrodynamical approach. Tectonophysics 148, 337–346.

Masuda, T., Mochizuki, S., 1989. Development of snowball structure: numerical simulation of inclusion trails during synkinematic porphyroblast growth in metamorphic rocks. Tectonophysics 170, 141–150.

Odonne, F., 1994. Kinematic behaviour of an interface and competence contrast: analogue models with different degrees of bonding between deformable inclusions and their matrix. Journal of Structural Geology 16, 997–1006.

Passchier, C.W., 1987. Stable position of rigid objects in non-coaxial flow—a study in vorticity analysis. Journal of Structural Geology 9, 679–690.

Passchier, C.W., Trouw, R.A.J., 1996. Microtectonics. Springer Verlag, New York.

Passchier, C.W., Trouw, A.J., Zwart, H.J., Vissers, R.L.M., 1992. Porphyroblast rotation: eppur si muove? Journal of Metamorphic Geology 10, 283–294.

Ramsay, J.G., Huber, M.I., 1983. The Techniques of Modern Structural Geology: Volume 1: Strain Analysis. Academic Press, London.

Rosenfeld, J.L., 1970. Rotated garnets in metamorphic rocks. Geological Society of America. Special Paper, 129.

Schoneveld, C., 1977. A study of some typical inclusion patters in strongly paracrystalline-rotated garnets. Tectonophysics 39, 453–471.

Shelton, G., Tullis, J., 1981. Experimental flow laws for crustal rocks. EOS, Transactions. American Geophysical Union 62, 369.

Shimamoto, T., 1975. The finite element analysis of the deformation of a viscous spherical body embeddded in a viscous medium. Journal of the Geological Society of Japan 81, 255–267.

Simpson, C., De Paor, D.G., 1993. Strain and kinematic analysis in general shear zones. Journal of Structural Geology 15, 1–20.

Spry, A., 1963. The origin and significance of snowball structure in garnet. Journal of Petrology 4, 221–222.

Tenczer, V., Stüwe, K., Barr, T., 2001. Pressure anomalies around cylindrical objects in simple shear. Journal of Structural Geology 23, 777–788.

Tullis, T.E., Horowitz, F.G., Tullis, J., 1991. Flow laws of polyphase aggregates from end-member flow laws. Journal of Geophysical Research 96, 8081–8096.

Visser, P., Mancktelow, N.S., 1992. The rotation of garnet porphyroblasts around a single fold, Lukmanier Pass, Central Alps. Journal of Structural Geology 14, 1193–1202.

Williams, P.F., Jiang, D., 1999. Rotating garnets. Journal of Metamorphic Geology 17, 367–378.

Williams, P.F., Schoneveld, C., 1981. Garnet rotation and the development of axial plane crenulation cleavage. Tectonophysics 78, 307–334.